Ground motions induced by vibration of a large-diameter end-bearing pile subjected to vertically distributed uniform loads

Yue, Cheng; Liu, Qijian; Zhao, Mingjuan

DOI
10.1016/j.soildyn.2025.109687

Publication date
2025

Document Version
Final published version

Published in
Soil Dynamics and Earthquake Engineering

Citation (APA)
Yue, C., Liu, Q., & Zhao, M. (2025). Ground motions induced by vibration of a large-diameter end-bearing pile subjected to vertically distributed uniform loads. *Soil Dynamics and Earthquake Engineering*, *199*, Article 109687. https://doi.org/10.1016/j.soildyn.2025.109687

Soil Dynamics and Earthquake Engineering 199 (2025) 109687

Contents lists available at ScienceDirect

Soil Dynamics and Earthquake Engineering

journal homepage: www.elsevier.com/locate/soildyn

Ground motions induced by vibration of a large-diameter end-bearing pile subjected to vertically distributed uniform loads

Cheng Yue [a], Qijian Liu [a,b,c,*], Mingjuan Zhao [d]

[a] College of Civil Engineering, Hunan University, Changsha, Hunan 410082, PR China
[b] Key Laboratory of Building Safety and Energy Efficiency of the Ministry of Education, Hunan University, Changsha, Hunan 410082, PR China
[c] State Key Laboratory of Bridge Safety and Resilience, Hunan University, Changsha, Hunan 410082, PR China
[d] Department of Structural Engineering, Delft University of Technology, Stevinweg 1, 2628CN Delft, The Netherlands

ARTICLE INFO

Keywords:
Ground motion
Pile vibration
Wave scattering
Soil–pile interaction
Continuum elasticity

ABSTRACT

This study develops a comprehensive analytical solution for predicting three-dimensional ground motions induced by the vibration of large-diameter end-bearing piles subjected to vertically distributed uniform loads. Both the pile and the surrounding soil are treated as elastic continuum media to capture the coupled effects of P-SV and Rayleigh waves accurately. General solutions for wave potentials, displacements, and stresses are derived using small-strain theory and continuum elasticity. Modal wave numbers are determined through a root-searching approach employing the argument principle and subdivision method. Bi-orthogonality relationships are reorganized using Betti's theorem. Soil–pile interactions are rigorously modeled through continuity conditions at the soil–pile interface. Mode-matching method is used to solve the unknown coefficients. The boundary-value problem is reduced to a system of linear algebraic equations with series truncation to ensure convergence and computational efficiency. Parametric studies reveal that excitation frequencies significantly influence the distribution of soil and pile responses. Shear waves corresponding to pile frictions dominate near-field responses and Rayleigh waves resulting from surface load propagate at larger distances. Transient displacement responses show the significant influence of complex Rayleigh wave propagation and the secondary subsurface scattering on the ground motions. The particle motions reveal the Rayleigh waves are generating and propagating through the ground surface induced by pile vibrating. This study contributes to the accurate prediction of ground motions and supports the design of vibrating grounds which ensures the safety of pile-supported structures in urban and displacement-sensitive environments.

1. Introduction

Pile foundations are widely used in civil and geotechnical engineering to support structures such as high-rise buildings, bridges, and offshore platforms [1–3]. Among various pile types, large-diameter end-bearing piles are increasingly employed due to their high load-bearing capacity and suitability for challenging ground conditions. However, the effect of pile vibrations induced by machinery or traffic loads and their impact on surrounding environments have not been studied sufficiently. When subjected to dynamic loads, piles vibrate and generate stress waves that propagate through the surrounding soil, leading to ground motions that can affect nearby structures and sensitive equipment [4]. These ground motions are particularly complex due to the coupling of P-SV waves and the propagation of Rayleigh waves, which results in both vertical and horizontal vibrations [5–8]. Accurate prediction of these coupled responses is crucial for ensuring the safety and functionality of both the supported structure and its surrounding environment.

Over the past decades, significant efforts have been made to model the dynamic response of piles. Analytical models, such as the plain-strain model [9–13], Tajimi model [14–19], Vlasov model [20–22], and Beam on Dynamic Winkler Foundation (BDWF) model [23–25], have been widely employed to evaluate the vertical and horizontal responses of pile shafts. Numerical methods, including the finite element method (FEM), finite difference method (FDM), and boundary element method (BEM) [26–30], have also been used to simulate piles embedded in layered or poroelastic media. Traditional approaches simplify the pile–soil interaction by neglecting the three-dimensional (3-D) wave effects and the spatial distribution of loads. However, these methods cannot reflect the three-dimensional response of the soil–pile system.

* Corresponding author.
E-mail address: Q.Liu@hnu.edu.cn (Q. Liu).

https://doi.org/10.1016/j.soildyn.2025.109687
Received 11 April 2025; Received in revised form 17 June 2025; Accepted 20 July 2025
Available online 1 August 2025

Recent studies have introduced 3-D models to better capture dynamic soil–pile interactions. In the pioneered studies, Liu et al. [31–33] proposed a three-dimensional model that accurately calculates the vertical response of piles and the associated vertical ground motions. However, their model can partially capture the horizontal ground motions, which are equally important due to the coupled P-SV waves and Rayleigh waves. The far-field ground motions cannot be accurately predicted owing to the relaxation of boundary conditions. Moreover, Tsouvalas and Metrikine [1–3,34] developed an analytical solution that considers three-dimensional wave effects. Their focus was primarily on underwater noise propagation rather than ground motions in geotechnical engineering. In the context of ground vibrations caused by pile driving, several empirical and semi-empirical models have been proposed to predict vibration levels based on factors such as hammer energy, pile properties, and soil conditions [35–38]. These models provide practical tools for estimating vibration amplitudes. However, they often rely on simplified assumptions, such as ignoring the soil's displacement vector or neglecting the three-dimensional wave propagation effects. Furthermore, most existing methods focus on vertical vibrations and fail to account for the coupled horizontal motions induced by P-SV and Rayleigh waves, which are critical for assessing the full impact of pile vibrating on surrounding structures or environments.

Despite these advances, there is a lack of comprehensive methods that can accurately analyze the coupled horizontal and vertical ground motions induced by pile vibrations [39,40]. To address these limitations, a comprehensive analytical model must be proposed to reveal three-dimensional ground motions induced by the vibration of large-diameter end-bearing piles.

In this study, the three-dimensional ground motions induced by pile vibrations are analyzed using wave propagation theory. Both the soil layer and pile foundation are modeled as elastic continuum media to accurately capture the coupled P-SV wave effects and Rayleigh wave propagation. Firstly, general solutions for the free-vibration field are derived using the method of variable separation, with fixed boundary conditions at the rigid base and traction-free conditions at the ground surface. Then, modal wave numbers are determined through a root-searching approach based on the argument principle and subdivision method. Furthermore, soil and pile responses are expressed as series solutions to capture the full three-dimensional wave effects. In addition, bi-orthogonality relations are reorganized using Betti's theorem to enforce continuity at the soil–pile interface. Moreover, the soil–pile interaction is solved using a matrix inversion approach inspired by the mode-matching method [41], reducing the boundary-value problem to a system of linear equations. Finally, a parametric study is conducted to explore the wave scattering effects on ground motions, providing new insights into the impact of soil–pile interactions on environmental vibrations.

2. The model

2.1. The problem

The configuration of the end-bearing pile embedded in a finite-depth elastic soil layer subjected to vertically distributed uniform loads and the coordinate system is depicted in Fig. 1. The soil is assumed to be homogeneous, isotropic and linearly elastic with Young's modulus E_s, Poisson's ratio ν_s, density ρ_s, Lamé constants $\mu_s = E_s/[2(1+\nu_s)]$ and $\lambda_s = 2\nu_s\mu_s/(1-2\nu_s)$, respectively. The end-bearing pile with a circular cross-section is embedded in the soil with length H, diameter D_p, and radius $R_p = D_p/2$, respectively. The pile is homogeneous, isotropic, and linearly elastic with Young's modulus E_p, density ρ_p, Poisson's ratio ν_p, Lamé constants $\mu_p = E_p/[2(1+\nu_p)]$ and $\lambda_p = 2\nu_p\mu_p/(1-2\nu_p)$, respectively. The time-harmonic vertical distributed uniform loads are expressed as $p_0e^{i\omega t}$ with amplitude p_0, imaginary unit $\mathrm{i} = \sqrt{-1}$, angular frequency

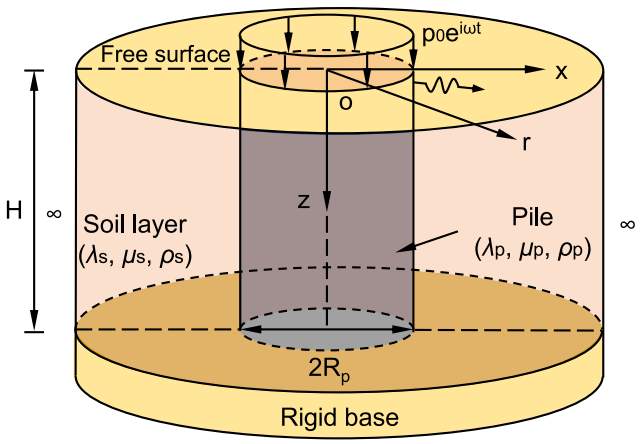

Fig. 1. The geometry of the proposed model.

$\omega = 2\pi f$, and frequency f in Hz. The time-harmonic factor $e^{i\omega t}$ will be understood and omitted in the ensuing analysis for brevity.

A semi-analytical solution for the soil–pile system can be obtained by decomposing the total response into two distinct components: the eigenfield response and the free-vibration response [41]. The eigenfield response refers to the part of the dynamic response that is directly induced by external dynamic vertical loads, characterizing how the system reacts to applied forces. In contrast, the free-vibration field describes the system's natural vibration modes, which are determined only by the material properties and geometric configuration of the soil–pile system. The free-vibration field exists independently of any external loading. By superposing these two components, the total displacement vector $\mathbf{u}^{(i)}$ and stress tensor $\boldsymbol{\sigma}^{(i)}$ of the soil–pile system can be expressed as

$$\mathbf{u}^{(i)}(r,z) = \mathbf{u}^{(i),e}(r,z) + \mathbf{u}^{(i),f}(r,z) \tag{1}$$

$$\boldsymbol{\sigma}^{(i)}(r,z) = \boldsymbol{\sigma}^{(i),e}(r,z) + \boldsymbol{\sigma}^{(i),f}(r,z) \tag{2}$$

where the subscripts e and f indicate the eigenfield and free-vibration field, respectively; the subscript $i = \{s,p\}$ denotes the soil and pile, respectively.

2.2. Basic assumptions

The following assumptions are introduced to simplify the considered problem:

(1) Both the pile shaft and the finite soil layer are modeled as homogeneous, isotropic and linearly elastic media;

(2) The total responses of soil and pile are divided into two parts as the eigenfield response and the free-vibration response, respectively;

(3) Vertical and radial displacements of the soil–pile system are considered simultaneously;

(4) The soil–pile system is regarded as an axisymmetric body to capture 3-D wave effects;

(5) Perfect contacts exist along the soil–pile slippages during small strain vibration. Continuous displacements and stress conditions are considered to formulate soil–pile interactions.

3. Problem formulation

3.1. Governing equations

The governing equation of the motions of soil and pile without body forces is [42]

$$(\lambda_i + \mu_i)\nabla\nabla\cdot\mathbf{u}^{(i)} + \mu_i\nabla^2\mathbf{u}^{(i)} = \rho_i\frac{\partial^2\mathbf{u}^{(i)}}{\partial t^2} \tag{3}$$

where λ_i and μ_i denote the Lamé's moduli of the soil or pile, respectively; ∇ is the gradient operator; ∇^2 denotes the Laplace operator; $\mathbf{u}^{(i)} = \{u_r^{(i)},\ u_z^{(i)}\}$ is the displacement vector of the soil or pile, respectively.

For the case of an axisymmetric problem, the displacement components $u_r^{(i)}$ and $u_z^{(i)}$ can be respectively expressed in terms of the scalar longitudinal wave potential $\phi^{(i)}$ and the scalar transverse wave potential $\chi^{(i)}$ by employing the Helmholtz decomposition via [2,31,43]

$$u_r^{(i)} = \frac{\partial \phi^{(i)}}{\partial r} + \frac{\partial^2 \chi^{(i)}}{\partial r \partial z} \tag{4}$$

$$u_z^{(i)} = \frac{\partial \phi^{(i)}}{\partial z} + (k_T^{(i)})^2 \chi^{(i)} + \frac{\partial^2 \chi^{(i)}}{\partial z^2} \tag{5}$$

where $k_T^{(i)} = \omega / v_T^{(i)}$ is the shear wave-number of the soil or pile, respectively; $v_T^{(i)} = \sqrt{\mu_i / \rho_i}$ is the transverse wave velocity of the soil or pile, respectively.

Once the displacements are expressed by wave potentials, the stress components $\sigma_{rr}^{(i)}$, $\sigma_{zz}^{(i)}$, and $\sigma_{rz}^{(i)}$ can be respectively expressed by Helmholtz's potentials $\phi^{(i)}$ and $\chi^{(i)}$ according to Hooke's law and small-strain elasticity as [42]

$$\sigma_{rr}^{(i)} = -\lambda_i (k_L^{(i)})^2 \phi^{(i)} + 2\mu_i \left(\frac{\partial^2 \phi^{(i)}}{\partial r^2} + \frac{\partial^3 \chi^{(i)}}{\partial r^2 \partial z} \right) \tag{6}$$

$$\sigma_{zz}^{(i)} = -\lambda_i (k_L^{(i)})^2 \phi^{(i)} + 2\mu_i \left(\frac{\partial^2 \phi^{(i)}}{\partial z^2} + (k_T^{(i)})^2 \frac{\partial \chi^{(s)}}{\partial z} + \frac{\partial^3 \chi^{(i)}}{\partial z^3} \right) \tag{7}$$

$$\sigma_{rz}^{(i)} = \sigma_{zr}^{(i)} = \mu_i \left(2\frac{\partial^2 \phi^{(i)}}{\partial r \partial z} + 2\frac{\partial^3 \chi^{(i)}}{\partial r \partial z^2} + (k_T^{(i)})^2 \frac{\partial \chi^{(i)}}{\partial r} \right) \tag{8}$$

where $k_L^{(i)} = \omega / v_L^{(i)}$ is the longitudinal wave number of the soil or pile, respectively; $v_L^{(i)} = \sqrt{(\lambda_i + 2\mu_i)/\rho_i}$ is the longitudinal wave velocity of the soil or pile, respectively.

Substituting Eqs. (4)~(5) into Eq. (3), the elastodynamic equilibrium equation of motions ignoring body force is reduced to two uncoupled scalar Helmholtz equations as

$$\frac{\partial^2 \phi^{(i)}}{\partial r^2} + \frac{1}{r}\frac{\partial \phi^{(i)}}{\partial r} + \frac{\partial^2 \phi^{(i)}}{\partial z^2} + (k_L^{(i)})^2 \phi^{(i)} = 0 \tag{9}$$

$$\frac{\partial^2 \chi^{(i)}}{\partial r^2} + \frac{1}{r}\frac{\partial \chi^{(i)}}{\partial r} + \frac{\partial^2 \chi^{(i)}}{\partial z^2} + (k_T^{(i)})^2 \chi^{(i)} = 0 \tag{10}$$

3.2. Free-field response

3.2.1. General solutions of the wave potentials

Solving Eq. (9) by separation of variables, the general solution for the free-vibration P wave potential $\phi^{(s),f}$ in the soil is

$$\phi^{(s),f}(r,\ z) = [A_1 \mathrm{H}_0^{(1)}(\xi^{(s)} r) + B_1 \mathrm{H}_0^{(2)}(\xi^{(s)} r)][C_1 \sin(p^{(s)} z) + D_1 \cos(p^{(s)} z)] \tag{11}$$

where A_1, B_1, C_1, and D_1 are the unknown coefficients, respectively; $\mathrm{H}_0^{(1)}(\cdot)$ and $\mathrm{H}_0^{(2)}(\cdot)$ are the Hankel function of order zero of the first (and second) kind, respectively; $\xi^{(s)}$ is the undetermined constant; $p^{(s)} = [(k_L^{(s)})^2 - (\xi^{(s)})^2]^{1/2}$ is an unknown wave-number variable related to P wave in the soil.

Likewise, the general solution of transverse wave potential $\chi^{(s),f}$ in the soil can be written as

$$\chi^{(s),f}(r,\ z) = [A_2 \mathrm{H}_0^{(1)}(\xi^{(s)} r) + B_2 \mathrm{H}_0^{(2)}(\xi^{(s)} r)][C_2 \sin(q^{(s)} z) + D_2 \cos(q^{(s)} z)] \tag{12}$$

where A_2, B_2, C_2, and D_2 are the unknown coefficients, respectively; $q^{(s)} = [(k_T^{(s)})^2 - (\xi^{(s)})^2]^{1/2}$ is an unknown wave-number variable related to S wave in the soil.

Furthermore, the fundamental solutions for Eqs. (9) and (10) of the free-vibration field in the pile can be written as

$$\phi^{(p),f}(r,\ z) = [A_3 \mathrm{J}_0(\xi^{(p)} r) + B_3 \mathrm{Y}_0(\xi^{(p)} r)][C_3 \sin(p^{(p)} z) + D_3 \cos(p^{(p)} z)] \tag{13}$$

$$\chi^{(p),f}(r,\ z) = [A_4 \mathrm{J}_0(\xi^{(p)} r) + B_4 \mathrm{Y}_0(\xi^{(p)} r)][C_4 \sin(q^{(p)} z) + D_4 \cos(q^{(p)} z)] \tag{14}$$

where A_3, B_3, C_3, D_3, A_4, B_4, C_4, and D_4 are the unknown coefficients, respectively; $\mathrm{J}_0(\cdot)$ and $\mathrm{Y}_0(\cdot)$ are the Bessel function of order zero and first or second kind, respectively; $\xi^{(p)}$ is the undetermined constant; $p^{(p)} = [(k_L^{(p)})^2 - (\xi^{(p)})^2]^{1/2}$ and $q^{(p)} = [(k_T^{(p)})^2 - (\xi^{(p)})^2]^{1/2}$ are the unknown wave-number variables related to P and S wave in the pile, respectively.

The Hankel and Bessel functions are respectively used to express the scattered wave potentials of soil and pile as shown in Eqs. (11)~(14). Both the Hankel functions and Bessel functions satisfy Helmholtz's Eqs. (9) and (10), and they present the cylindrical waves in the soil and pile. The choice of Hankel or Bessel function is based on the physical characteristics of the soil–pile system. There are only outgoing scattered waves in the soil. However, both incoming and outgoing waves exist in the pile foundation. Meanwhile, since the pile volume under consideration encloses the origin, radial dependence must be restricted to Bessel functions. Hence, it is convenient to respectively use Hankel function $\mathrm{H}_0^{(2)}(\cdot)$ for wave potentials of soil with time factor $e^{\mathrm{i}\omega t}$, while using Bessel function $\mathrm{J}_0(\cdot)$ for the pile to present the wave fields. Due to the outgoing scattered waves resulting from the pile vibration and the radiation conditions along the r-axis, the constants $A_1 = A_2 = 0$ are determined in Eqs. (11) and (12). Meanwhile, elastic waves in the pile concerning the radial coordinate result in limited values along the radius from the origin. Hence, the constants $B_3 = B_4 = 0$ are determined in Eqs. (13) and (14).

3.2.2. Boundary conditions and eigenvalue problem

For the pile and soil layer with finite depth H, boundary conditions along the half-surface and the rigid base should be incorporated to consider the eigenvalue problem. For displacement-fixed rigid base ($z = H$), the boundary conditions are

$$u_r^{(i),f}|_{z=H} = 0, \qquad u_z^{(i),f}|_{z=H} = 0 \quad (i = s,\ p) \tag{15}$$

Traction-free boundaries along the half-surface ($z = 0$) lead to

$$\sigma_{zz}^{(i),f}|_{z=0} = 0, \qquad \sigma_{zr}^{(i),f}|_{z=0} = 0 \quad (i = s,\ p) \tag{16}$$

Substituting Eqs. (4)~(5), (7)~(8), and (11)~(14) into boundary conditions Eqs. (15)~(16), and noting $(\lambda_i + 2\mu_i)(k_L^{(i)})^2 = \mu_i (k_T^{(i)})^2$, it yields

$$\mathbf{L}^{(i)} \mathbf{X}^{(i)} = 0 \quad (i = s,\ p) \tag{17}$$

where $\mathbf{X}^{(s)} = \{C_1,\ D_1,\ C_2,\ D_2\}^{\mathrm{T}}$ and $\mathbf{X}^{(p)} = \{C_3,\ D_3,\ C_4,\ D_4\}^{\mathrm{T}}$ are the vectors containing unknown coefficients, respectively; the superscript $\{\}^{\mathrm{T}}$ denotes the transpose of matrix; $\mathbf{L}^{(i)}$ $(i = s,\ p)$ can be expressed as

$$\mathbf{L}^{(i)} = \begin{bmatrix} \sin(p^{(i)}H) & \cos(p^{(i)}H) & q^{(i)}\cos(q^{(i)}H) & -q^{(i)}\sin(q^{(i)}H) \\ p^{(i)}\cos(p^{(i)}H) & -p\sin(p^{(i)}H) & (\xi^{(i)})^2 \sin(q^{(i)}H) & (\xi^{(i)})^2 \cos(q^{(i)}H) \\ 0 & 2(\xi^{(i)})^2 - (k_T^{(i)})^2 & 2q^{(i)}(\xi^{(i)})^2 & 0 \\ 2p^{(i)} & 0 & 0 & 2(\xi^{(i)})^2 - (k_T^{(i)})^2 \end{bmatrix} \tag{18}$$

Eq. (18) forms a linear system of algebraic equations. For a non-trivial solution, the determinants of coefficients matrices should be zero as $\det[\mathbf{L}^{(i)}] = 0$, which leads to [44]

$$\begin{aligned} D(\xi^{(i)}) = {} & 4p^{(i)}q^{(i)}(\xi^{(i)})^2[2(\xi^{(i)})^2 - (k_T^{(i)})^2] \\ & + (\xi^{(i)})^2\{[2(\xi^{(i)})^2 - (k_T^{(i)})^2]^2 + 4(p^{(i)})^2(q^{(i)})^2\}\sin(p^{(i)}H)\sin(q^{(i)}H) \\ & - p^{(i)}q^{(i)}\{[2(\xi^{(i)})^2 - (k_T^{(i)})^2]^2 + 4(\xi^{(i)})^4\}\cos(p^{(i)}H)\cos(q^{(i)}H) = 0 \end{aligned} \tag{19}$$

where $D(\xi^{(i)}) = \det[\mathbf{L}^{(i)}]$ is the determinant functions.

This requirement provides a set of modal wave-numbers $\xi_n^{(i)}, (i = s, p)$ with $n = 1, 2, \ldots$ for each excitation frequency. Meanwhile, the value of modal wave numbers should be specified due to their physical characteristics. To comply with the radiation condition and the condition of finite response at an infinite distance away from the soil–pile

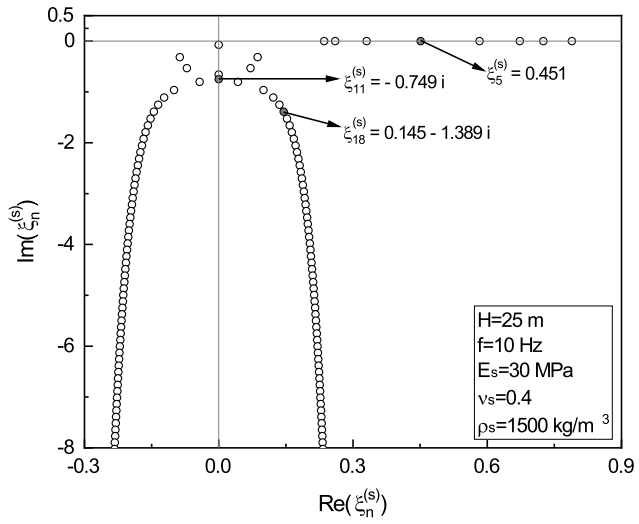

Fig. 2. Roots of the determinant equation of a soil layer in the range $[-0.3, 0.9] + i[-3, 0.5]$ (including 8 real-valued roots, 3 imaginary-valued roots, and 38 complex-valued roots).

interface, only the complex-valued roots that lie in the lower complex half-plane ($\mathrm{Im}(\xi_n^{(i)}) \le 0$) are incorporated. For the real-valued roots, $\mathrm{Re}(\xi_n^{(i)}) > 0$ should be taken for $\omega > 0$, implying positive phase velocities.

To determine all the roots of determinant function Eq. (19), a combination of the argument principle (or Cauchy's argument principle) and the subdivision method is employed [45–47]. The procedure begins with an initial search for roots along the real and imaginary axes using Newton's method [48]. The argument principle is then applied to compute the number of roots within a specified region of the fourth quadrant of the complex plane [49]. If the number of roots in the region is greater than one, the region is subdivided into smaller regions for further analysis. If the root count in a region equals zero, no further search is conducted in that area. For regions containing exactly one root, Newton's method is used to refine the root's location. Finally, the roots in the third quadrant are set as the conjugates of the roots found in the fourth quadrant. This method ensures that the total number and locations of all roots in the complex plane are accurately identified. The argument principle is used to quantify root presence, the subdivision method is employed to isolate regions with roots, and Newton's method is further adopted to refine root values. Finding 200 complex-valued roots requires only 30 s and 1 GB of RAM. Compared to previous fixed-grid approaches, the present method requires fewer computational resources and less time, while still maintaining mathematical rigor.

Fig. 2 shows the example arrangements of modal wave numbers $\xi_n^{(s)}$ in the complex plane with given parameters. An infinite number of complex-valued roots exists and only the roots with $\mathrm{Im}(\xi_n^{(s)}) \le -3$ are displayed in Fig. 2. Also, the complex roots are located at two branches positioned symmetrically concerning the imaginary axis, which is attributed to the homogeneity of the soil layer. Even for the layered ground, the arrangement of modal wave numbers are still symmetrical [2]. The real part of the complex-valued roots is much smaller than the imaginary part and therefore these modes decay fast with increasing radial distance. Physically speaking, the real-valued roots correspond to modes that propagate in the r direction, while the complex roots relate to modes that decay with distance from the soil–pile interface [41,50].

The determinant function Eq. (19) provides the relationship between the unknown coefficients C_1, D_2, C_2 and D_2 in Eqs. (11)~(12). Once the modal wave-number $\xi_n^{(s)}$ is determined, four coefficients can be solved directly. Then the other three coefficients D_1, C_2, and D_2 in Eqs. (11) and (12) can be expressed by C_1. Similarly, coefficients C_3, D_3, C_4 and D_4 in Eqs. (13)~(14) can be obtained when $\xi_n^{(p)}$ is known. Any three out of four coefficients can be subsequently solved for each $\xi_n^{(i)}$ ($n = 1, 2, 3, \ldots$) in terms of a series of single unknown complex constants A_m or B_n. Then, substituting the modal wave numbers $\xi_n^{(i)}$ into the Helmholtz potentials Eqs. (11)~(14), the resulting expressions for displacements $u_r^{(i),f}$ and $u_z^{(i),f}$ of the soil and pile can be respectively written in a series form as

$$u_r^{(s),f}(r,\ z) = \sum_{m=1}^{\infty} A_m \mathrm{H}_1^{(2)}(\xi_m^{(s)} r) U_m^{(s)}(z) \tag{20}$$

$$u_z^{(s),f}(r,\ z) = \sum_{m=1}^{\infty} A_m \mathrm{H}_0^{(2)}(\xi_m^{(s)} r) W_m^{(s)}(z) \tag{21}$$

$$u_r^{(p),f}(r,\ z) = \sum_{n=1}^{\infty} B_n \mathrm{J}_1(\xi_n^{(p)} r) U_n^{(p)}(z) \tag{22}$$

$$u_z^{(p),f}(r,\ z) = \sum_{n=1}^{\infty} B_n \mathrm{J}_0(\xi_n^{(p)} r) W_n^{(p)}(z) \tag{23}$$

where $U_n^{(i)}(z)$ ($i = s,\ p$) and $W_n^{(i)}(z)$ are respectively the eigenfunctions for displacements of soil and pile as listed in Appendix A, respectively.

Meanwhile, stresses components $\sigma_r^{(i),f}$ and $\sigma_{rz}^{(i),f}$ of the soil and pile can be respectively expressed according to Hooke's law as

$$\sigma_{rr}^{(s),f}(r,\ z) = \sum_{m=1}^{\infty} A_m \left[\mathrm{H}_0^{(2)}(\xi_m^{(s)} r) \Gamma_{rr1,m}^{(s)}(z) + \frac{1}{r}\mathrm{H}_1^{(2)}(\xi_m^{(s)} r) \Gamma_{rr2,m}^{(s)}(z)\right] \tag{24}$$

$$\sigma_{zz}^{(s),f}(r,\ z) = \sum_{m=1}^{\infty} A_m \mathrm{H}_0^{(2)}(\xi_m^{(s)} r) \Gamma_{zz,m}^{(s)}(z) \tag{25}$$

$$\sigma_{rz}^{(s),f}(r,\ z) = \sum_{m=1}^{\infty} A_m \mathrm{H}_1^{(2)}(\xi_m^{(s)} r) \Gamma_{rz,m}^{(s)}(z) \tag{26}$$

$$\sigma_{rr}^{(p),f}(r,\ z) = \sum_{n=1}^{\infty} B_n \left[\mathrm{J}_0(\xi_n^{(p)} r) \Gamma_{rr1,n}^{(p)}(z) + \frac{1}{r}\mathrm{J}_1(\xi_n^{(p)} r) \Gamma_{rr2,n}^{(p)}(z)\right] \tag{27}$$

$$\sigma_{zz}^{(p),f}(r,\ z) = \sum_{n=1}^{\infty} B_n \mathrm{J}_0(\xi_n^{(p)} r) \Gamma_{zz,n}^{(p)}(z) \tag{28}$$

$$\sigma_{rz}^{(p),f}(r,\ z) = \sum_{n=1}^{\infty} B_n \mathrm{J}_1(\xi_n^{(p)} r) \Gamma_{rz,n}^{(s)}(z) \tag{29}$$

where $\Gamma_{rr1,n}^{(i)}(z)$, $\Gamma_{rr2,n}^{(i)}(z)$, $\Gamma_{zz,n}^{(i)}(z)$, and $\Gamma_{rz,n}^{(i)}(z)$ are the eigenfunctions for stresses of soil and pile as listed in Appendix A, respectively.

3.3. Eigenfield response

The eigenfields of piles excited by the vertical dynamic loads were derived in the previous study [10,31]. Because the vertically distributed uniform loads are only applied on the pile, the pressure can be treated as the body force along the depth. Meanwhile, there are no eigenfields for the soil layer due to the traction-free conditions along the free boundary of the soil. The amplitude of the discrete excitation force p_0 acting at the pile head may be expanded in Fourier series $P(z)$ as [10]

$$P(z) = \frac{2p_0}{H} \sum_{n=1}^{\infty} \cos(h_n z) \tag{30}$$

where $h_n = (2n-1)\pi/(2H)$ ($n = 1, 2, \ldots$) are the constants; n is positive integer.

Meanwhile, the governing equation for eigenfield response considering vertical displacement $u_z^{(p),e}(z)$ is

$$(\lambda_p + 2\mu_p)\frac{\partial^2 u_z^{(p),e}(z)}{\partial z^2} + P(z) = -\rho_p \omega^2 u_z^{(p),e}(z) \tag{31}$$

In this contribution, the eigen-displacements $u_r^{(p),e}$ and $u_z^{(p),e}$ can be respectively written as

$$u_r^{(p),e}(z) = 0 \tag{32}$$

$$u_z^{(p),e}(z) = \frac{2p_0}{H} \sum_{n=1}^{\infty} \frac{\cos(h_n z)}{-\rho_p \omega^2 + (\lambda_p + 2\mu_p) h_n^2} \tag{33}$$

Combining Eqs. (32)~(33) and the Hooke's law, the eigen-stresses $\sigma_{rz}^{(p),e}$ and $\sigma_{zz}^{(p),e}$ are

$$\sigma_{rz}^{(p),e}(z) = 0 \tag{34}$$

$$\sigma_{rr}^{(p),e}(z) = -\frac{2p_0}{H}\sum_{n=1}^{\infty}\frac{\lambda_p h_n \sin(h_n z)}{-\rho_p\omega^2 + (\lambda_p + 2\mu_p)h_n^2} \tag{35}$$

4. Solution technique

4.1. Continuity conditions along the soil–pile interface

After the derivation of fundamental solutions of the soil–pile system, the dynamic response of the soil and pile can be respectively obtained by numerical calculation of the matrices involving unknown coefficients. The boundary-valued problem can be regarded as the continuity conditions along the interfaces of the soil–pile slippage as

$$u_r^{(p)} = u_r^{(s)}, \quad u_z^{(p)} = u_z^{(s)} \quad (r = R_p) \tag{36}$$

$$\sigma_r^{(p)} = \sigma_r^{(s)}, \quad \sigma_{rz}^{(p)} = \sigma_{rz}^{(s)} \quad (r = R_p) \tag{37}$$

Substituting Eqs. (1)~(2) into Eqs. (36)~(37), the continuity conditions lead to

$$u_r^{(s),f}(R_p, z) - u_r^{(p),f}(R_p, z) = u_r^{(p),e}(z) \tag{38}$$

$$u_z^{(s),f}(R_p, z) - u_z^{(p),f}(R_p, z) = u_z^{(p),e}(z) \tag{39}$$

$$\sigma_{rr}^{(s),f}(R_p, z) - \sigma_{rr}^{(p),f}(R_p, z) = \sigma_{rr}^{(p),e}(z) \tag{40}$$

$$\sigma_{rz}^{(s),f}(R_p, z) - \sigma_{rz}^{(p),f}(R_p, z) = \sigma_{rz}^{(p),e}(z) \tag{41}$$

Eqs. (38)~(41) indicates that there are four different continuity conditions along the soil–pile interface. However, the free-vibration fields of soil and pile only contain two sets of unknown coefficients A_m and B_n in Eqs. (20)~(29). Former investigations set the numbers of boundary conditions and unknown coefficients to be identical which ensures the calculation efficiency according to orthogonality of Fourier series mode-by-mode [31–33,51]. In this study, the eigenfunctions along the z-axis are the combinations of trigonometric functions, and cannot satisfy the orthogonality relationships straightforwardly. Hence, it is essential to derive the modal orthogonality relations to restrict the calculation of soil–pile interactions.

4.2. Modal orthogonality relation

An approximate linear combination of the wave potentials gives a relation between the unknown modal coefficients of the scattered wave potentials in soil or pile. For the displacement and stress expressions of the soil and pile including eigenfunctions, there exist orthogonality relations of the modal wave-numbers. We now wish to investigate the physical significance of the normalization of eigenfunctions in a cylinder geometry.

The energy flux for a single outgoing Fourier–Bessel component of the wave field (modal wave-number $\xi_n^{(i)}$) should be examined to consider the modal orthogonality relations. The energy flux due to the real part of the displacement field through the surface S of the cylinder and averaged over a single period is given by [50,52]

$$\int_S [\mathbf{u}\cdot\mathbf{T}(\mathbf{v}) - \mathbf{v}\cdot\mathbf{T}(\mathbf{u})]\cdot\mathbf{n}\mathrm{d}S = 0 \tag{42}$$

where $\mathbf{u}$ and $\mathbf{v}$ are the displacement vector on the surface S; $\mathbf{T}(\cdot)$ denotes the stress tensor resulted by displacement vector; $\mathbf{n}$ is the unit normal vector on S.

Since traction vanishes at the free surface ($z = 0$) and displacement tends to be zero at the rigid base ($z = H$), only the flux over the vertical surface with a radius $r = a$ exists [2,44,50,52]. Substituting Eqs. (20)~(29) into Eq. (42), and taking $\mathbf{u}$ and $\mathbf{v}$ as displacement vectors with modal wave-numbers $\xi_m^{(i)}$ and $\xi_n^{(i)}$, it is straightforward that the integral Eq. (42) satisfies the bi-orthogonality relation as [53]

$$\begin{aligned}\int_0^H \Big[&(\lambda_i + 2\mu_i)U_m^{(i)}(z)\cdot\xi_n^{(i)}U_n^{(i)}(z) + \mu_i\xi_m^{(i)}W_m^{(i)}(z)\cdot W_n^{(i)}(z) \\ &+\lambda_i U_m^{(i)}(z)\frac{\partial W_n^{(i)}(z)}{\partial z} - \mu_i\frac{\partial U_m^{(i)}(z)}{\partial z}W_n^{(i)}(z)\Big]\mathrm{d}z = N_n^{(i)}\delta_{mn}\end{aligned} \tag{43}$$

where $N_n^{(i)}$ is the norm of eigenfunction; δ_{mn} is the Kronecker delta.

The eigenfunctions in z-direction (e.g., Eqs. (A.1)~(A.6) in Appendix A) remain unaltered in both cases and therefore the bi-orthogonality condition is exactly equivalent for any combinations. Thus, another form of bi-orthogonality relations must be built for cylindrical waveguides in this study [2,50]. Therefore, substituting Eqs. (A.1)~(A.6) into Eq. (43), the bi-orthogonality relation between displacement eigenfunctions can be re-organized in the form of the combination of displacement and stress eigenfunctions via

$$\int_0^H \left[U_m^{(i)}(z)\Gamma_{rr1,n}^{(i)}(z) - \Gamma_{rz,m}^{(i)}(z)W_n^{(i)}(z)\right]\mathrm{d}z = N_n^{(i)}\delta_{mn} \tag{44}$$

$$\begin{aligned}\int_0^H \Big\{ &\Gamma_{rr2,m}^{(i)}(z)\xi_n^{(i)}U_n^{(i)}(z) - U_m^{(i)}(z)[\eta_i\Gamma_{zz,n}^{(i)}(z) + \varpi_i\xi_n^{(i)}U_n^{(i)}(z)] \\ &+\Gamma_{rz,m}^{(i)}(z)W_n^{(i)}(z)\Big\}\mathrm{d}z = -N_n^{(i)}\delta_{mn}\end{aligned} \tag{45}$$

where $\eta_i = \lambda_i/(\lambda_i + 2\mu_i), (i = s, p)$ and $\varpi_i = 2\lambda_i\mu_i/(\lambda_i + 2\mu_i)$ are the constants, respectively.

4.3. Matrix equation for solving the coupled problem

Based on the bi-orthogonality relations, the boundary conditions in Eqs. (38)–(41) are combined into a single integral expression (weak formulation) to link the known modal coefficients of the soil and pile [2,54]. At this point, two admissible combinations with the bi-orthogonality relations should be used according to the different stress components. Hence, multiplying both sides of Eq. (38) by $\Gamma_{rr1,n}^{(s)}(z)$, both sides of Eq. (41) by $-W_n^{(s)}(z)$, then sum and integral two equations between $[0, H]$; Meanwhile, multiplying both sides of Eq. (40) by $U_n^{(p)}(z)$, both sides of Eq. (39) by $-\Gamma_{rz,n}^{(p)}(z)$, both side of Eq. (38) by $-[\eta_p\Gamma_{zz,n}^{(p)}(z) + \varpi_p\cdot\xi_n^{(p)}U_n^{(p)}(z)]/(\xi_n^{(p)}R_p)$, both sides of Eq. (41) by $W_n^{(p)}(z)/(\xi_n^{(p)}R_p)$, then sum and integral four equations between $[0, H]$, we obtain

$$A_m Q_m^{(1)} - \sum_{l=1}^{\infty} B_l S_{ml}^{(1)} = T_m^{(1)} \tag{46}$$

$$\sum_{k=1}^{\infty} A_k S_{kn}^{(2)} - B_n Q_n^{(2)} = T_n^{(2)} \tag{47}$$

where $Q_m^{(1)}$, $S_{ml}^{(1)}$, $T_m^{(1)}$, $Q_{kn}^{(2)}$, $S_n^{(2)}$ and $T_n^{(2)}$ are the matrix elements listed in Appendix B, respectively.

According to Eq. (47), the unknown coefficients B_n can be expressed in terms of A_k as

$$B_n = \frac{1}{Q_n^{(2)}}\left(\sum_{k=1}^{\infty} A_k S_{kn}^{(2)} - T_n^{(2)}\right) \tag{48}$$

replacing n by l and substituting Eq. (48) into Eq. (46), we obtain an equation with the only unknown modal coefficients as

$$A_m - \frac{1}{Q_m^{(1)}}\sum_{k=1}^{\infty} A_k \sum_{l=1}^{\infty}\frac{S_{kl}^{(2)}S_{ml}^{(1)}}{Q_l^{(2)}} = \frac{1}{Q_m^{(1)}}\left(T_m^{(1)} - \sum_{l=1}^{\infty}\frac{T_l^{(2)}S_{ml}^{(1)}}{Q_l^{(2)}}\right) \tag{49}$$

Eq. (49) can be written as the matrix form as

$$\mathbf{G}\cdot\mathbf{A} = \mathbf{R} \tag{50}$$

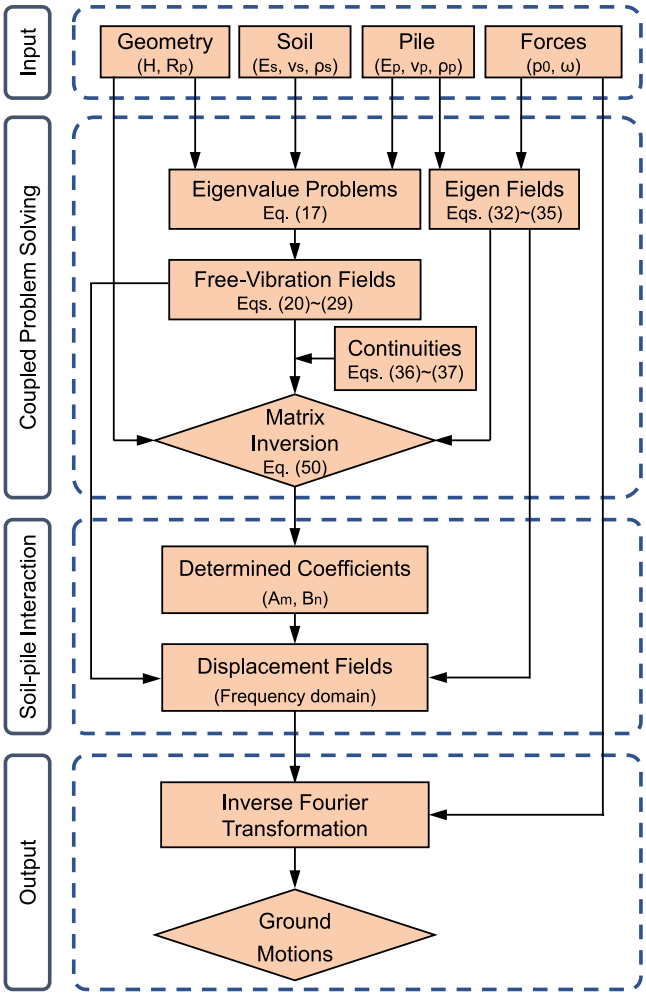

Fig. 3. Algorithm of the present model.

where $\mathbf{A} = \{A_1, A_2, \ldots, A_m\}^{\mathrm{T}}$ is the vector with unknown coefficients; $\mathbf{G}$ is a $m \times k$ matrix; $\mathbf{R}$ is a $m \times 1$ vector; the entries in $\mathbf{G}$ and $\mathbf{R}$ are

$$G_{m,k} = \delta_{mk} - \frac{1}{Q_m^{(1)}} \sum_{l=1}^{\infty} \frac{S_{kl}^{(2)} S_{ml}^{(1)}}{Q_l^{(2)}} \tag{51}$$

$$R_m = \frac{1}{Q_m^{(1)}} \left(T_m^{(1)} - \sum_{l=1}^{\infty} \frac{T_l^{(2)} S_{ml}^{(1)}}{Q_l^{(2)}} \right) \tag{52}$$

Eq. (49) contains a series of linear algebraic equations concerning the unknown coefficients A_m. After obtaining A_m, the unknown coefficients B_n can be straightforwardly calculated according to the modal relationship Eq. (48). Fig. 3 shows the diagram of the solution technique, which presents the computational method and simulation process.

5. Convergence tests and validations

5.1. Convergence tests

The accuracy and convergence of the present solution depend strongly on the choice of the series truncation numbers m and n. In numerical calculations, these series are truncated to prescribed values M and N, respectively. Fig. 4 presents the convergence tests for the radial displacement $|u_r^{(s)}(10R_p, 0)|$ at the free surface of the soil layer. Various values of M and N are considered with different slenderness ratios H/D_p and modulus ratios E_p/E_s. The geometric and material parameters used in the analysis are: $H = 20$ m, $p_0 = 100$ kPa, $f = 10$ Hz, $\rho_s = 1792$ kg/m^3, $\rho_p = 2500$ kg/m^3, $\nu_p = 0.2$, $\nu_s = 0.4$ and $E_p = 30$ GPa. The series truncation numbers for the soil and pile are set equal, i.e., $M = N$. Fig. 4(a) adopts a slenderness ratio of $H/D_p = 10$, and soil's modulus E_s varies. Fig. 4(b) uses a modulus ratio of $E_p/E_s = 100$ and pile diameter D_p varies. As shown in Fig. 4, satisfactory convergence is achieved for both low and high values of the slenderness and modulus ratios. To ensure the reliability and accuracy of the results, $M = N = 100$ are adopted in the ensuing analysis. All results for a given frequency can be computed within 5 min on a computer with Windows 10 21H1 environment, a 3.50 GHz AMD® R9-3950X CPU, and 64.00 GB RAM.

5.2. Validations

To verify the accuracy of the proposed method, we compare the results of our solution with those of two examples. The first example is the pile response under vertically distributed uniform loads, as presented by [10,31]. The second example involves the results of ground motions in soil resulting from pile vibrations by FEM simulations and 3-D model [31].

Fig. 5 compares the vertical displacements of the pile calculated using the proposed method with the results from previous studies [10, 31]. The following geometry and material parameters are used for the comparison: $p_0 = 10$ kPa, $H = 20$ m, $\rho_s = 1800$ kg/m^3, $\nu_s = 0.4$, $E_s = 30$ MPa, $E_p = 300$ MPa, $\rho_p = 2500$ kg/m^3, $\nu_p = 0.2$, $f = 1$ Hz, respectively. Good agreements of pile response can be observed by the results of the present solution with those of the available methods. Comparisons between the present results and those of [10,31] reveal that this method reflects the three-dimensional wave effect in the analysis of dynamic pile response under vertical loads.

Fig. 6 shows the comparisons of radial and vertical displacements of the soil layer by the proposed method with FEM simulations and previous study [31]. In the comparison, the following geometry and material property parameters are adopted: $p_0 = 1$ kPa, $H = 20$ m, $R_p = 1$ m, $\rho_s = 1800$ kg/m^3, $\nu_s = 0.4$, $E_s = 1$ MPa, $\rho_p = 2500$ kg/m^3, $\nu_p = 0.2$, $f = 1$ Hz, respectively. The maximum element size of the FEM model is chosen as 1.0 m, which is less than one-tenth of the soil wavelength associated with the input dynamic loads [55]. Rayleigh damping is applied on all the soil and pile elements. The mass-proportional constant is $\alpha = 0.001$, the stiffness-proportional constant is $\beta = 1$ Hz [56]. In the model, a large radius of the soil layer ($r = 100R_p$) and absorbing boundaries are applied to the surrounding boundaries to avoid spurious wave reflections into the model. The absorbing boundary involves dashpots attached independently to the boundary in the normal and shear directions. Viscous terms are introduced directly into the equations of motion of the grid points lying on the boundary [57]. Radial and vertical displacements at the bottom surface are fixed to simulate the rigid base. Stresses are applied in the normal direction at the top surface within $r \le R_p$ to formulate vertically distributed uniform loads. As shown in Fig. 6, good agreements are obtained between the results of the present solution and the FEM modeling.

The accuracy and robustness of the present analytical framework are demonstrated through validation against both FEM simulations and existing solutions, as shown in Figs. 5 and 6. Fig. 5 reveals that the existing solutions can accurately model the vertical pile response. However, there are some inaccuracies in the radial displacements in the shallow region of the soil layer after relaxation [31]. This approximation has minimal impact on the vertical response of the pile but has a more significant effect on the neighboring soil ground motion. The present analytical method accurately captures both horizontal and vertical ground motion characteristics, even in far-field regions ($r = 10R_p$). The continuum elasticity formulation used in the present model rigorously satisfies all boundary conditions, including traction-free surfaces, rigid-base constraints, and perfect bonding at the soil–pile

Table 1
Differences between the proposed method and the existing models.

Model	Soil model	Pile model	Pile responses		Ground motions	
			Vertical	Radial	Vertical	Radial
Present model	Continuum media	Continuum media	✓	✓	✓	✓
Nogami & Novák [10]	1-D model	1-D beam element	✓		✓	
Wu et al. [32]	3-D model	1-D beam element	✓		✓	
Tsouvalas & Metrikine [2]	Continuum media	1-D shell element	✓		✓	✓
Liu et al. [31]	3-D model	3-D model	✓	✓	✓	

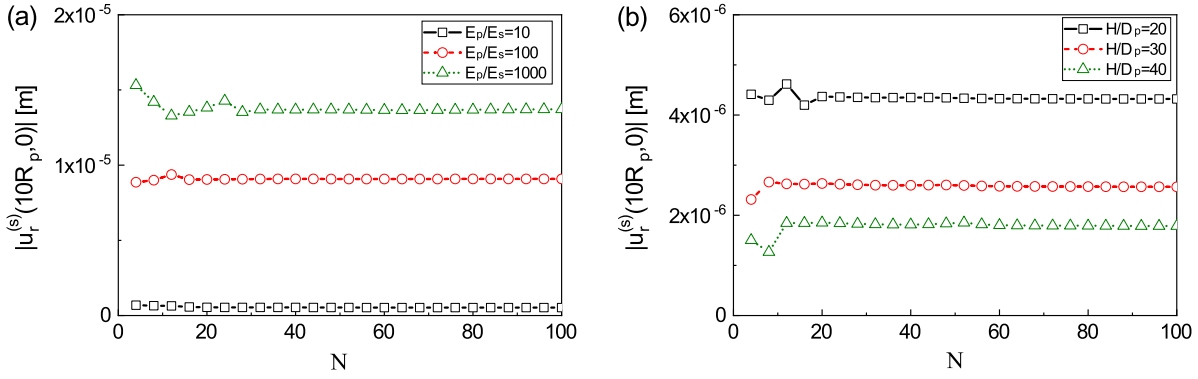

Fig. 4. Convergence test on the influence of truncation numbers M and N ($M = N$) of complex-valued modal wave-number on the radial displacement $|u_r^{(s)}(10R_p, 0)|$ at the free-surface.

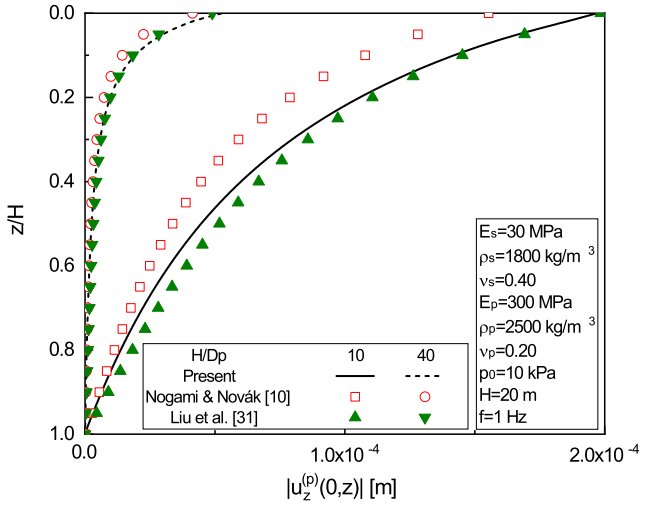

Fig. 5. Comparisons of vertical pile responses by the proposed solution with those of [10,31].

interface. This mathematical completeness ensures that the model accounts for coupled P–S wave propagation, radial-vertical displacement coupling, and energy radiation into the far field. The agreement with FEM results underscores the model's potential as a benchmark for evaluating simplified methods or numerical algorithms. Furthermore, it is beneficial to compare the proposed method to that of existing models for vertical pile vibrations [2,10,31,32]. Their relations and differences are summarized and clarified on a point-by-point basis as

Table 1 summarizes the differences among various analytical methods. Nogami and Novák [10] modeled the pile as a one-dimensional rod and neglected the radial displacements of the soil to simplify the soil–pile system analysis. However, omitting the soil's radial displacements introduces inaccuracies in the prediction of pile impedance. To address this, Wu et al. [32] employed three-dimensional wave theory to account for the radial soil displacements. Nonetheless, their approach still models the pile as an elastic 1-D rod. This assumption can be inaccurate for piles with a small slenderness ratio (H/D_p). Further advancement was made by Liu et al. [31], who treated both the pile and soil as three-dimensional continua, thereby fully capturing the wave effects. However, both Wu's and Liu's methods relaxed the soil layer boundary conditions because their primary focus was on pile impedance. This relaxation can result in significant errors when predicting three-dimensional ground motions. In contrast, Tsouvalas and Metrikine [2] developed a rigorous continuum theory that considers all boundary conditions of the soil and accurately describes three-dimensional wave scattering. Despite this, the pile is still represented as a shell element, which imposes limitations. To overcome these issues, the present method formulates both the soil and pile as three-dimensional continua. This approach enables the determination of all displacement tensors and ground motions with greater accuracy.

6. Results and discussions

In this section, a parametric study will be conducted to investigate the effects of waves on soil–pile interactions and induced ground motions. If not mentioned specially, the pile parameters are selected as $H = 20$ m, $R_p = 1$ m, $E_p = 30$ GPa, $\rho_p = 2500$ kg/m^3, and $\nu_p = 0.30$, respectively. For the surrounding soil, the material properties are $E_s = 333.65$ MPa, $\rho_s = 1792$ kg/m^3, $\nu_s = 0.4895$, and the corresponding wave velocities are $v_T^{(s)} = 250.00$ m/s, $v_L^{(s)} = 1743.19$ m/s and Rayleigh wave velocity $v_R^{(s)} = 238.50$ m/s, respectively. The soil with the aforementioned wave velocities corresponds to sandy soil or clay soil. It is convenient to introduce the non-dimensional displacements $\bar{u}_r$ and $\bar{u}_z$ as

$$\bar{u}_r^{(i)} = \frac{u_r^{(i)}}{u_0}, \quad \bar{u}_z^{(i)} = \frac{u_z^{(i)}}{u_0} \tag{53}$$

where $u_0 = p_0 \pi R_p^2/(\mu_p H)$.

Fig. 7 illustrates the dimensionless vertical and horizontal displacement amplitudes $|\bar{u}_r^{(s)}|$ and $|\bar{u}_z^{(s)}|$ of soil layer for different load frequencies. Fig. 7(a) indicates that the lateral displacements are prominent near the ground surface and at mid-depth of the soil layer at low frequencies. While vertical displacements attenuate rapidly with radial distance. Specifically, horizontal motions persist even at large distances from the pile origin ($r = 40R_p$), whereas vertical motions

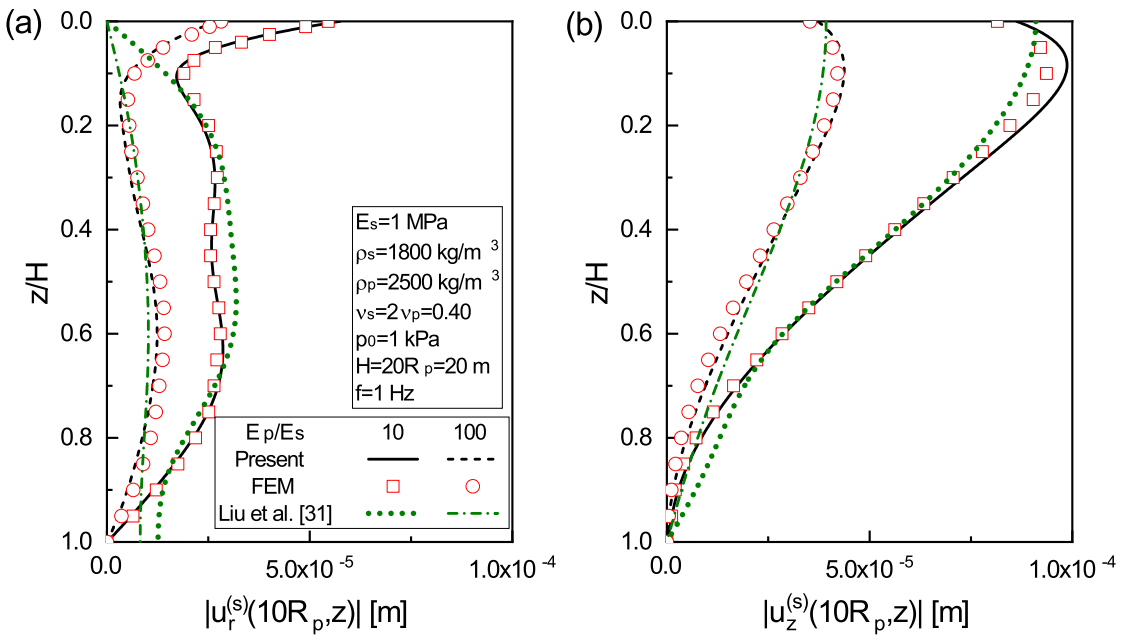

Fig. 6. Comparisons of $|u_r^{(s)}|$ and $|u_z^{(s)}|$ by the proposed solution with FEM results and [31].

concentrate within a narrow range ($r = 3R_p$). This behavior can be attributed to the fact that low-frequency loads induce long-wavelength vibrations capable of propagating energy over long distances into the surrounding soil. The rapid attenuation of vertical displacements is due to the radiation effects in the vertical direction. As shown in Figs. 7(b)~(d), standing waves and displacement peaks grow in the soil layer as the excitation frequency increases ($20 \sim 40$ Hz). This phenomenon may result from localized soil resonance or inertial effects. When high-frequency oscillations coincide with the natural vibration modes of the soil, energy concentrates in the soil near the vibrating source. These peaks and resonances indicate the activation of higher-order wave modes or reflections from layer boundaries, revealing the frequency-dependent complexity of wave propagation paths.

Although soil motions in the frequency domain are crucial for capturing dynamic concentration points, it is also meaningful to explore ground motions in the time domain. Transient analysis provides valuable insights into dynamic wave propagation in the soil layer and the diffraction of waves at the ground surface. In this study, the transient response of the soil layer is derived from steady-state analysis using the fast inverse Fourier transform (IFFT) technique. The calculated frequencies range from 0 Hz to 64 Hz in 1/2 Hz intervals, resulting in a 2-second time window with 1/64-second time intervals. The vertical impulse load is simulated by a symmetric Ricker wavelet and defined as

$$p(t) = p_0 \left(1 - 2\pi^2 f_c^2 t^2\right) \exp\left(-\pi^2 f_c^2 t^2\right) \tag{54}$$

where f_c is the characteristic frequency of the wavelet and is selected to be 10 Hz.

Fig. 8 presents the synthesized horizontal and vertical displacement time histories of the soil surface for different radial distances, reconstructed using the IFFT technique. At small radial distances, the horizontal displacement is relatively small compared to the more pronounced vertical displacement as Fig. 8(b). This indicates that impulsive vertical loads primarily generate shear wave motions, which dominate the near-field response. The vertical displacement rapidly decays after the initial pulse and sharply diminishes with increasing radial distance. This behavior is attributed to the swift attenuation of P- and S-waves due to soil radiation-damping effects. When vertical loads are applied on the pile head, the pile moves up and down, which generates transverse waves at the soil–pile interface. Meanwhile, the pile will also expand radially due to the three-dimensional wave effect. Then, the P-waves will be induced. This phenomenon is associated with the Poisson's ratio of pile. Hence, the P-waves are the result of Poisson's ratio, and the S-waves correspond to the friction along the soil–pile interface. In contrast, both horizontal and vertical displacements exhibit impulsive peaks at larger radial distances, which maintain measurable magnitudes over an extended duration. This remarkable far-field response aligns with Rayleigh wave propagation mechanisms in the soil layer, which efficiently transport energy over longer distances. These observations highlight the complex interplay between near-field wave attenuation and far-field wave dispersion in soil–pile interaction systems. The alteration in displacement patterns further emphasizes the importance of directional dynamic analysis for accurate seismic assessments. Also, additional investigations of detailed ground motion responses in the time domain should be explored to investigate the wave propagation induced by pile vibrating.

Fig. 9 shows the horizontal and vertical displacements at the ground surface ($z = 0$ m, $r = 100$ m) over a time window of 2 seconds. When a vertical impulse load is applied to the pile head, it generates both P and S waves within the soil layer. The P waves are associated with horizontal displacements, while the S waves correspond to vertical ground motions. As shown in Fig. 9, peak displacements occur in the solids, with the first peak in radial motion linked to the P head wave and the first peak in vertical displacements associated with the S head wave. Following the propagation of these P and S waves, Rayleigh waves are induced by the surface impulse load on the pile head. Notably, the ground motions caused by the P and S head waves are significantly smaller than those produced by the Rayleigh waves. This observation indicates that P and S waves attenuate rapidly as radial distance increases, whereas Rayleigh waves propagate through the soil with greater energy transmission. Additionally, it is noteworthy that oscillations in ground motions persist after the propagation of the Rayleigh waves.

The subsequent oscillations in the displacement curves after the Rayleigh wave passage arise from the complex interaction between Rayleigh wave propagation and subsurface scattering as Fig. 10. Specifically, as Rayleigh waves propagate outward from the soil–pile interface, their energy propagates along the soil surface while simultaneously diffracting downward to the rigid base at depth. Upon reaching the soil-bedrock interface, these waves are partially scattered back

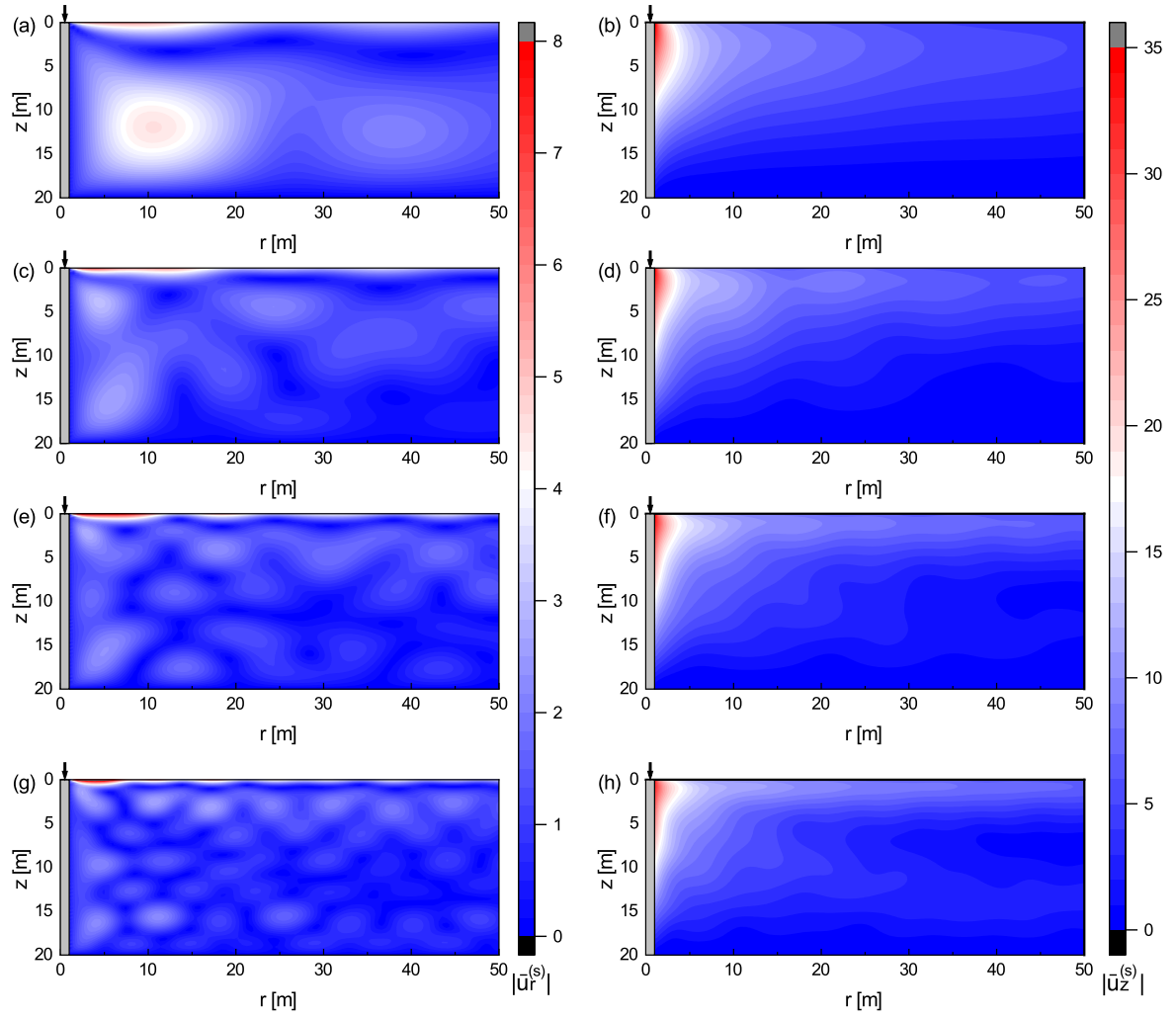

Fig. 7. Contours of non-dimensional radial and vertical displacements for different load frequencies: $f = 10$ Hz for (a) and (b), $f = 20$ Hz for (c) and (d), $f = 30$ Hz for (e) and (f), $f = 40$ Hz for (g) and (h).

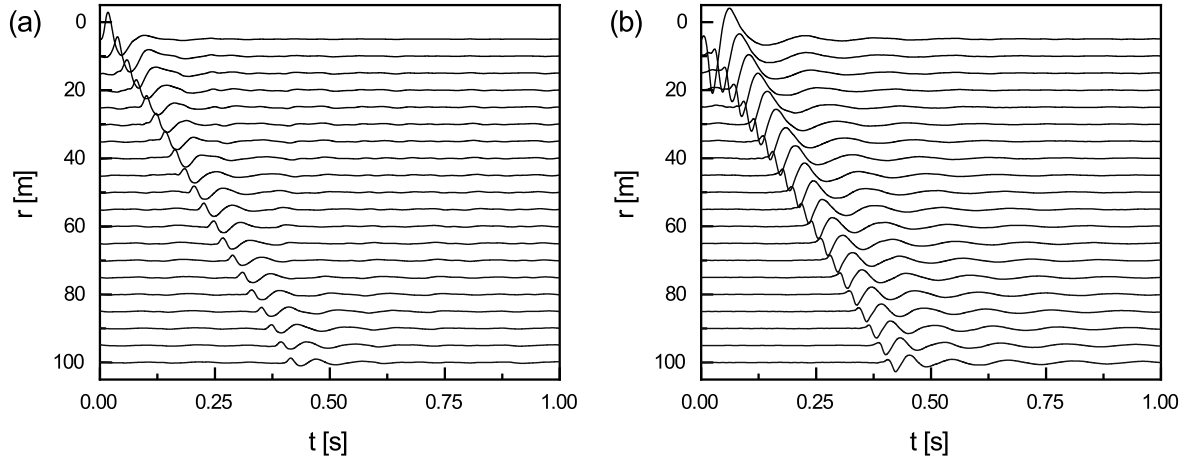

Fig. 8. Synthetic non-dimensional displacements along the half surface ($z = 0$ m) for different radial distances: (a) Horizontal displacements $\bar{u}_r^{(s)}$ and (b) Vertical displacements $\bar{u}_z^{(s)}$.

toward the surface. This scattering process introduces secondary wave fields that interfere with the primary Rayleigh wave, generating oscillatory patterns in the displacement records [58]. Furthermore, the persistent oscillations observed in Fig. 9 after the main Rayleigh wave pulse result from multiple scattering events between the rigid base and the free surface. Each reflection at the base reintroduces delayed wave energy to the surface, creating overlapping phases that manifest as prolonged low-amplitude vibrations. These effects illustrate the long-term ground motion behavior in the soil layer affected by boundary conditions.

Figs. 11~12 illustrate the horizontal and vertical displacement contours within the soil layer under transient vertical loading. The contours

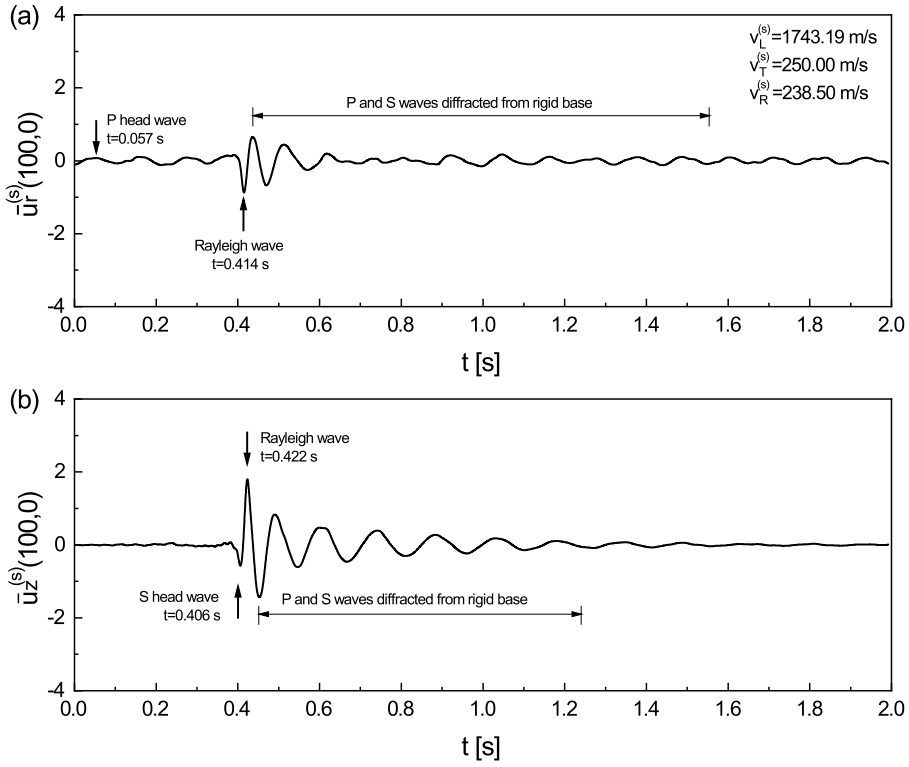

Fig. 9. Time histories of non-dimensional horizontal and vertical displacements $\bar{u}_r^{(s)}$ and $\bar{u}_z^{(s)}$ at $(r,\ z) = (100,\ 0)$ m.

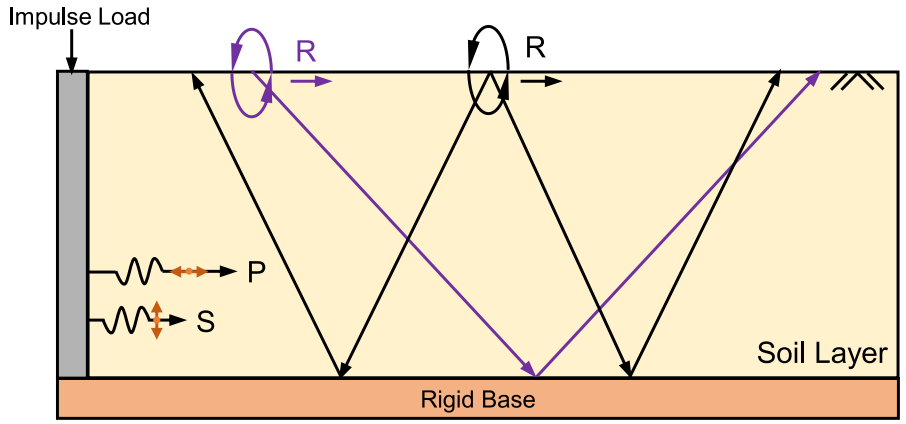

Fig. 10. Wave propagation in the soil layer.

reveal the complex interaction between wave propagation and interference phenomena. Initially, P- and S-head waves emerge and travel rapidly through the soil layer, followed by the remarkable Rayleigh waves at the surface. As these Rayleigh waves propagate outward from the soil–pile interface, they not only travel along the surface but also penetrate deeper into the soil. When the propagating waves reach the rigid base, the wave potentials are reflected and diffracted by the surface as shown in Figs. 11(d) and 12(d).

The interaction between the direct Rayleigh waves and the secondary scattered waves leads to constructive displacement amplitudes, resulting in spatial variations in the ground motions. This wave interaction governs the dynamic response of the soil medium and influences the distribution of stresses and strains in the soil surrounding the pile. The presence of the pile causes localized energy dissipation due to scattering and damping effects, which may lead to a faster decay of Rayleigh wave amplitude in the vicinity of the pile compared to areas farther away. This localized energy dissipation is critical for understanding the soil–pile interaction and its effect on ground motion.

Since the Rayleigh waves resulting from pile vibrating are indicated by Figs. 8∼10, it is meaningful to explore the Rayleigh wave propagation in the soil layer. Fig. 13 illustrates soil particle motions under transient pile vibration in the time domain. It is well known that the particle motion is elliptical retrograde near the surface and elliptical prograde at a greater depth for propagating Rayleigh waves. Fig. 13 reveals that the particle motions exhibit a counterclockwise retrograde elliptical motion at the free surface, which is attributed to the dominance of Rayleigh waves. With increasing depth, the particle motions reverse to a clockwise prograde motion, reflecting the phase inversion of Rayleigh wave components below the surface. The surface displacements decay slowly. In contrast, deeper soil displacements attenuate quickly with increasing radial distance. This phenomenon corresponds to the Rayleigh waves traveling along the soil surface and the body waves (P- and S-waves) propagating through the soil layer. The body waves exert a significant influence on the soil motion close to the soil–pile interface. However, the Rayleigh waves become the

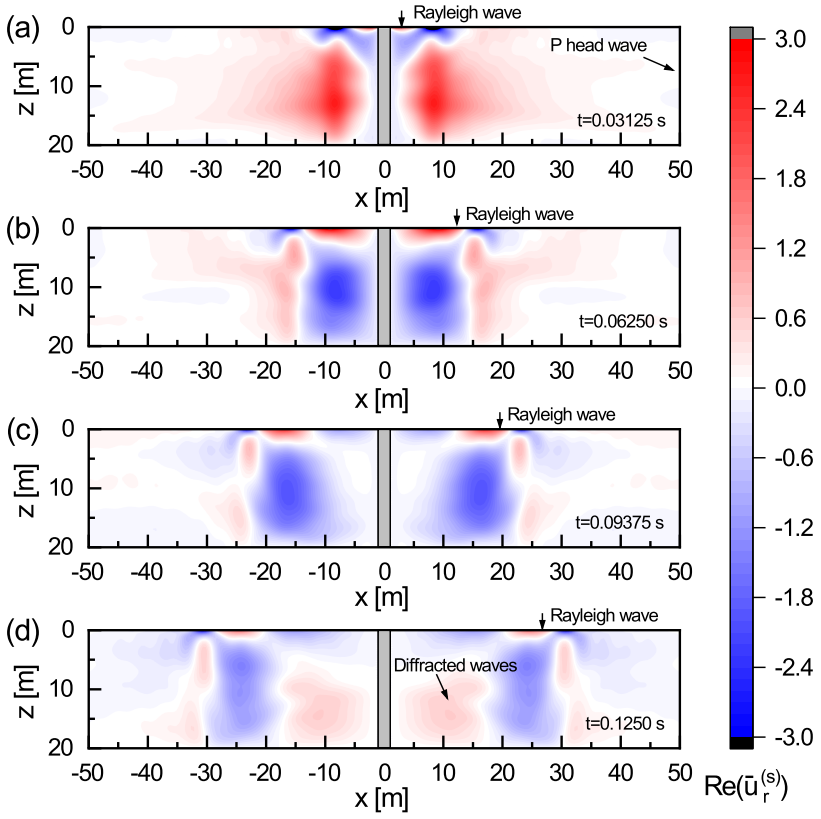

Fig. 11. Contours of non-dimensional vertical displacements.

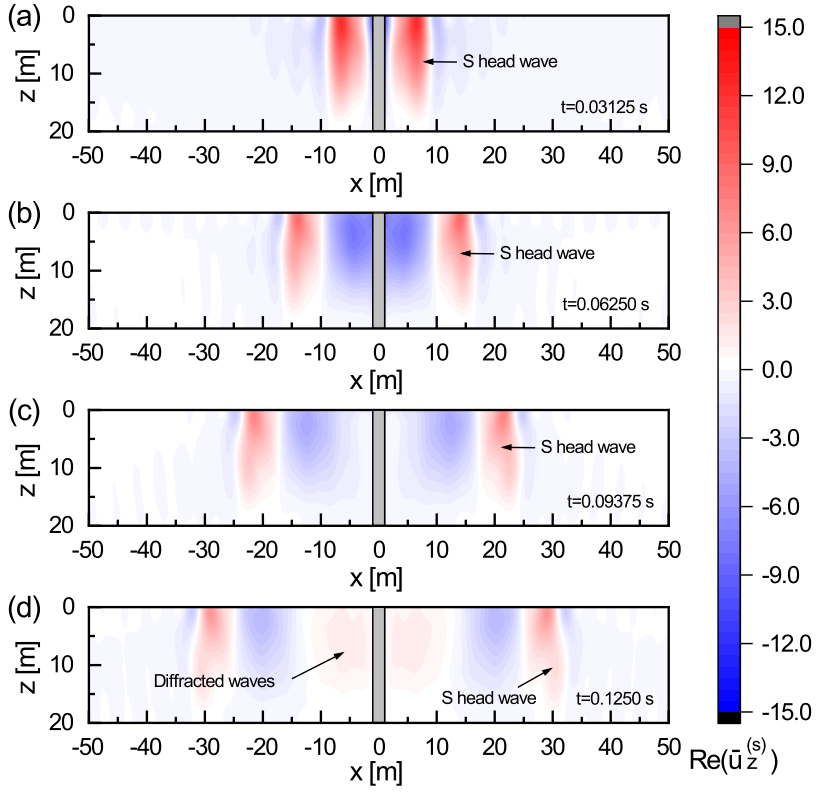

Fig. 12. Contours of non-dimensional vertical displacements.

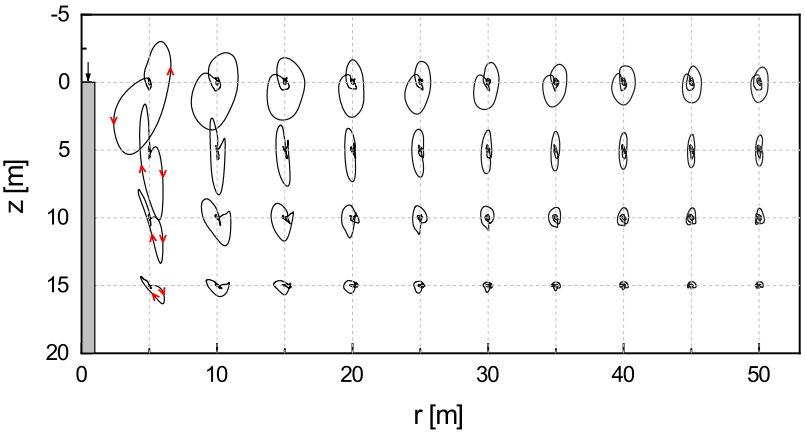

Fig. 13. Particle motions of the soil layer in the time domain.

dominant force in the soil's response at the far-field ground surfaces. This transition is crucial to nearby structures located at considerable distances from the vibrating pile. The resulting ground motions can have profound effects on their stability and integrity due to propagating Rayleigh waves and diffracted waves.

7. Conclusions

An analytical solution for the dynamic response of soil–pile systems subjected to vertically distributed uniform loads has been developed. The solution incorporates three-dimensional wave effects and captures the coupled interactions between the soil and pile. The governing equations of soil and pile are solved using Helmholtz's decomposition and method of variable separations. The eigenvalue problems are formulated to construct a series solution of Helmholtz's wave potentials. Modal orthogonality relations are reorganized due to Betti's theorem. The boundary value problem is formulated as an infinite linear algebraic system by considering continuity conditions along the soil–pile interface. The proposed method offers a robust and efficient framework for predicting ground motions during pile driving assessments, offshore pile vibration, and dynamic machine operations.

The analytical solution developed in this study serves as an exact and efficient tool for investigating the dynamic response of soil–pile interactions under vertical loads. By accurately modeling the three-dimensional wave effects, this method offers valuable insights into the complex behavior of soil–pile systems and can serve as a benchmark for validating numerical simulations. It also enhances the theoretical understanding of dynamic soil–pile interactions, particularly in impulse responses. A parametric study has been conducted to explore the wave effects of soil–pile systems and the induced ground motions. The following conclusions are drawn:

(1) Excitation frequencies play a critical role in the distribution of soil and pile responses. At low frequencies, horizontal displacements are more pronounced and can propagate over long distances into the surrounding soil. In contrast, higher frequencies lead to more localized displacements with standing waves and resonance effects observed in the soil layer. These findings emphasize the importance of frequency-dependent behavior in dynamic response assessments.

(2) Radial distance from the pile significantly affects the dynamic response of the soil. At close radial distances, impulsive vertical loads generate strong shear wave motions, which dominate the near-field response. At larger radial distances, Rayleigh waves become the primary mode of energy propagation, leading to more sustained displacements. This transition underscores the importance of careful site planning for displacement-sensitive equipment. It is suggested that such equipment be installed at a distance of at least one Rayleigh wavelength from the vibrating pile to minimize potential adverse effects.

(3) Soil–pile interface effects are crucial in determining the overall ground motion characteristics. The study shows that the interaction between the pile and surrounding soil influences the distribution of displacements and stresses, especially in the near-field regions.

These findings underscore the complex interactions between pile geometry, soil properties, and dynamic wave effects. The results provide critical insights into accurate predictions of ground motions. The dynamic response of the soil layer induced by pile vibrating is essential for ensuring structural safety and minimizing seismic risks.

This paper focuses on the ground motions induced by the vibration of an end-bearing pile in a homogeneously elastic half-space. It is unable to solve the ground motions in poroelastic or layered medium with this method. The present method can be expanded to a floating pile embedded in the layered or poroelastic medium by employing the matrix transform method and Biot's theorem. Compared to existing methods, present analytical solution can serve as a benchmark to ensure the accuracy and efficiency of numerical methods.

CRediT authorship contribution statement

Cheng Yue: Writing – original draft, Validation, Software, Methodology, Formal analysis. **Qijian Liu:** Writing – original draft, Supervision, Methodology, Conceptualization. **Mingjuan Zhao:** Writing – review & editing, Methodology, Formal analysis.

Declaration of competing interest

The authors declare that they have no known competing financial interests or personal relationships that could have appeared to influence the work reported in this paper.

Acknowledgments

The study was supported by the National Natural Science Foundation of China under Grant Nos. 52178331 and 52478340. The authors were grateful to Prof. Dr. Peter G. Malischewsky and Dr. Karel N. van Dalen for their constructive comments which enhanced the quality of this manuscript. The authors were also grateful to the anonymous Reviewers for their constructive comments, which significantly improved the manuscript.

Appendix A. Eigenfunctions for soil and pile

Eigenfunctions for the soil and pile in Eqs. (20)~(29) can be respectively written as

$$U_n^{(i)}(z) = -\xi_n^{(i)}[\sin(p_n^{(i)}z) + \alpha_n^{(i)}\cos(p_n^{(i)}z) + \beta_n^{(i)}q_n^{(i)}\cos(q_n^{(i)}z) - \gamma_n^{(i)}q_n^{(i)}\sin(q_n^{(i)}z)] \tag{A.1}$$

$$W_n^{(i)}(z) = p_n^{(i)}\cos(p_n^{(i)}z) - \alpha_n^{(i)}p_n^{(i)}\sin(p_n^{(i)}z) + \beta_n^{(i)}(\xi_n^{(i)})^2\sin(q_n^{(i)}z) + \gamma_n^{(i)}(\xi_n^{(i)})^2\cos(q_n^{(i)}z) \tag{A.2}$$

$$\Gamma_{rr1,n}^{(i)}(z) = (\lambda_i + 2\mu_i)\xi_n^{(i)}U_n^{(i)}(z) + \lambda_i\frac{\partial W_n^{(i)}(z)}{\partial z} \tag{A.3}$$

$$\Gamma_{rr2,n}^{(i)}(z) = -2\mu_i U_n^{(i)}(z) \tag{A.4}$$

$$\Gamma_{zz,n}^{(i)}(z) = (\lambda_i + 2\mu_i)\frac{\partial W_n^{(i)}(z)}{\partial z} + \lambda_i\xi_n^{(i)}U_n^{(i)}(z) \tag{A.5}$$

$$\Gamma_{rz,n}^{(i)}(z) = \mu_i\frac{\partial U_n^{(i)}(z)}{\partial z} - \mu_i\xi_n^{(i)}W_n^{(i)}(z) \tag{A.6}$$

where $p_n^{(i)} = [(k_L^{(i)})^2 - (\xi_n^{(i)})^2]^{1/2}$ and $q_n^{(i)} = [(k_T^{(i)})^2 - (\xi_n^{(i)})^2]^{1/2}$ are the constants with corresponding values of $\xi^{(i)} = \xi_n^{(i)}$, respectively; $\alpha_n^{(i)}$, $\beta_n^{(i)}$, and $\gamma_n^{(i)}$ are respectively the complex constants as

$$\alpha_n^{(i)} = -\frac{2(\xi_n^{(i)})^2}{2(\xi_n^{(i)})^2 - (k_T^{(i)})^2}\cdot\frac{[2(\xi_n^{(i)})^2 - (k_T^{(i)})^2]\sin(p_n^{(i)}H) + 2p_n^{(i)}q_n^{(i)}\sin(q_n^{(i)}H)}{2(\xi_n^{(i)})^2\cos(p_n^{(i)}H) - [2(\xi_n^{(i)})^2 - (k_T^{(i)})^2]\cos(q_n^{(i)}H)} \tag{A.7}$$

$$\beta_n^{(i)} = -\alpha_n^{(i)}\frac{2(\xi_n^{(i)})^2 - (k_T^{(i)})^2}{2(\xi_n^{(i)})^2 q_n^{(i)}} \tag{A.8}$$

$$\gamma_n^{(i)} = -\frac{2p_n^{(i)}}{2(\xi_n^{(i)})^2 - (k_T^{(i)})^2} \tag{A.9}$$

Appendix B. Elements of matrices

Matrix elements in Eqs. (51)~(52) are

$$Q_m^{(1)} = N_m^{(s)}\mathrm{H}_1^{(2)}(\xi_m^{(s)}R_p) \tag{B.1}$$

$$S_{ml}^{(1)} = \mathrm{J}_1(\xi_l^{(p)}R_p)\int_0^H\left[U_l^{(p)}(z)\Gamma_{rr1,m}^{(s)}(z) - \Gamma_{rz,l}^{(p)}(z)W_m^{(s)}(z)\right]\mathrm{d}z \tag{B.2}$$

$$T_m^{(1)} = 0 \tag{B.3}$$

$$Q_n^{(2)} = N_n^{(p)}\left[\mathrm{J}_0(\xi_n^{(p)}R_p) - \frac{\mathrm{J}_1(\xi_n^{(p)}R_p)}{\xi_n^{(p)}R_p}\right] \tag{B.4}$$

$$\begin{aligned} S_{kl}^{(2)} = {} & \mathrm{H}_0^{(2)}(\xi_k^{(s)}R_p)\int_0^H\left[\Gamma_{rr1,k}^{(s)}(z)U_l^{(p)}(z) - W_k^{(s)}(z)\Gamma_{rz,l}^{(p)}(z)\right]\mathrm{d}z \\ & + \frac{\mathrm{H}_1^{(2)}(\xi_k^{(s)}R_p)}{\xi_l^{(p)}R_p}\int_0^H\left[\Gamma_{rr2,k}^{(s)}(z)\xi_l^{(p)}U_l^{(p)}(z) + \Gamma_{rz,k}^{(s)}(z)W_l^{(p)}(z)\right. \\ & \left. - U_k^{(s)}(z)\left(\eta_p\Gamma_{zz,l}^{(p)}(z) + \varpi_p\xi_l^{(p)}U_l^{(p)}(z)\right)\right]\mathrm{d}z \end{aligned} \tag{B.5}$$

$$T_l^{(2)} = \int_0^H\left[\sigma_{rr}^{(p),e}(z)U_l^{(p)}(z) - u_z^{(p),e}(z)\Gamma_{rz,l}^{(p)}(z)\right]\mathrm{d}z \tag{B.6}$$

Data availability

No data was used for the research described in the article.

References

[1] Molenkamp T, Tsetas A, Tsouvalas A, Metrikine AV. Underwater noise from vibratory pile driving with non-linear frictional pile–soil interaction. J Sound Vib 2024;576:118298. http://dx.doi.org/10.1016/j.jsv.2024.118298.

[2] Tsouvalas A, Metrikine AV. A three-dimensional vibroacoustic model for the prediction of underwater noise from offshore pile driving. J Sound Vib 2014;333(8):2283–311. http://dx.doi.org/10.1016/j.jsv.2013.11.045.

[3] Tsouvalas A, Metrikine A. Noise reduction by the application of an air-bubble curtain in offshore pile driving. J Sound Vib 2016;371:150–70. http://dx.doi.org/10.1016/j.jsv.2016.02.025.

[4] Grizi A, Athanasopoulos-Zekkos A, Woods RD. Ground vibration measurements near impact pile driving. J Geotech Geoenviron Eng 2016;142(8):04016035. http://dx.doi.org/10.1061/(ASCE)GT.1943-5606.0001499.

[5] Gazetas G. Analysis of machine foundation vibrations: State of the art. Int J Soil Dyn Earthq Eng 1983;2(1):2–42. http://dx.doi.org/10.1016/0261-7277(83)90025-6.

[6] Kim D, Lee J. Propagation and attenuation characteristics of various ground vibrations. Soil Dyn Earthq Engi 2000;19(2):115–26. http://dx.doi.org/10.1016/S0267-7261(00)00002-6.

[7] Ainalis D, Kaufmann O, Tshibangu J, Verlinden O, Kouroussis G. Modelling the source of blasting for the numerical simulation of blast-induced ground vibrations: A review. Rock Mech Rock Eng 2017;50:171–93. http://dx.doi.org/10.1007/s00603-016-1101-2.

[8] Huang JK, Shi ZF. Attenuation zones of periodic pile barriers and its application in vibration reduction for plane waves. J Sound Vib 2013;332(19):4423–39. http://dx.doi.org/10.1016/j.jsv.2013.03.028.

[9] Kuo K, Hunt H. An efficient model for the dynamic behaviour of a single pile in viscoelastic soil. J Sound Vib 2013;332(10):2549–61. http://dx.doi.org/10.1016/j.jsv.2012.12.023.

[10] Nogami T, Novák M. Soil-pile interaction in vertical vibration. Earthq Eng Struct Dyn 1976;4(3):277–93. http://dx.doi.org/10.1002/eqe.4290040308.

[11] Novák M, Nogami T. Soil-pile interaction in horizontal vibration. Earthq Eng Struct Dyn 1977;5(3):263–81. http://dx.doi.org/10.1002/eqe.4290050305.

[12] Novák M, Aboul-Ella F, Nogami T. Dynamic soil reactions for plane strain case. J Eng Mech Div 1978;104(4):953–9. http://dx.doi.org/10.1061/JMCEA3.0002392.

[13] El Naggar M, Novák M. Non-linear model for dynamic axial pile response. J Geotech Eng 1994;120(2):308–29. http://dx.doi.org/10.1061/(ASCE)0733-9410(1994)120:2(308).

[14] Anoyatis G, Lemnitzer A. Dynamic pile impedances for laterally–loaded piles using improved Tajimi and Winkler formulations. Soil Dyn Earthq Eng 2017;92:279–97. http://dx.doi.org/10.1016/j.soildyn.2016.09.020.

[15] Zheng CJ, Kouretzis G, Ding XM. Analysis of laterally loaded floating piles using a refined tajimi model. Int J Numer Anal Methods Geomech 2024;48:2727–44. http://dx.doi.org/10.1002/nag.3753.

[16] Zheng CJ, Kouretzis G, Ding XM. Dynamic response of floating piles subjected to axial loads considering three-dimensional soil deformations. Comput Geotech 2023;154:105144. http://dx.doi.org/10.1016/j.compgeo.2022.105144.

[17] Anoyatis G, Di Laora R, Lemnitzer A. Dynamic pile impedances for fixed-tip piles. Soil Dyn Earthq Eng 2017;97:454–67. http://dx.doi.org/10.1016/j.soildyn.2017.03.025.

[18] Cui CY, Liang ZM, Xu CS, Xin Y, Wang BL. Analytical solution for horizontal vibration of end-bearing single pile in radially heterogeneous saturated soil. Appl Math Model 2023;116:65–83. http://dx.doi.org/10.1016/j.apm.2022.11.027.

[19] Cui CY, Qi YF, Meng K, You ZJ, Liang ZM, Xu CS. A new analytical solution for horizontal vibration of floating pile in saturated soil based on FSSP method. Soil Dyn Earthq Eng 2024;187:108960. http://dx.doi.org/10.1016/j.soildyn.2024.108960.

[20] Gupta BK. On the Vlasov-Leont'ev foundation model for axial dynamic stiffness of a pile embedded in a viscoelastic soil. J Earthq Eng 2024;1–24. http://dx.doi.org/10.1080/13632469.2024.2325007.

[21] Gupta BK. Lateral dynamics of a pile in a homogeneous half-space with Vlasov–Leont'ev foundation model and expressions for a rigid disk. Int J Geomech 2024;24(2):04023268. http://dx.doi.org/10.1061/IJGNAI.GMENG-853.

[22] Cao G, Wang X, He CD. Dynamic analysis of a laterally loaded rectangular pile in multilayered viscoelastic soil. Soil Dyn Earthq Eng 2023;165:107695. http://dx.doi.org/10.1016/j.soildyn.2022.107695.

[23] Cesaro R, Di Laora R. An analytical solution for the filtering effect of piles in two-layer soil. Soil Dyn Earthq Eng 2023;175:108273. http://dx.doi.org/10.1016/j.soildyn.2023.108273.

[24] Gazetas G, Fan K, Kaynia A. Dynamic response of pile groups with different configurations. Soil Dyn Earthq Eng 1993;12(4):239–57. http://dx.doi.org/10.1016/0267-7261(93)90061-U.

[25] He R, Kaynia AM. Winkler spring coefficients for laterally loaded piles. Comput Geotech 2024;170:106264. http://dx.doi.org/10.1016/j.compgeo.2024.106264.

[26] Padrón L, Aznárez J, Maeso O. BEM–FEM coupling model for the dynamic analysis of piles and pile groups. Eng Anal Bound Elem 2007;31(6):473–84. http://dx.doi.org/10.1016/j.enganabound.2006.11.001.

[27] Millán M, Domínguez J. Simplified BEM/FEM model for dynamic analysis of structures on piles and pile groups in viscoelastic and poroelastic soils. Eng Anal Bound Elem 2009;33(1):25–34. http://dx.doi.org/10.1016/j.enganabound.2008.04.003.

[28] Wu GX, Finn W. Dynamic nonlinear analysis of pile foundations using finite element method in the time domain. Can Geotech J 1997;34(1):44–52. http://dx.doi.org/10.1139/t96-088.

[29] Messioud S, Okyay US, Sbartai B, Dias D. Dynamic response of pile reinforced soils and piled foundations. Geotech Geol Eng 2016;34:789–805. http://dx.doi.org/10.1007/s10706-016-0003-0.

[30] Kaynia AM, Kausel E. Dynamics of piles and pile groups in layered soil media. Soil Dyn Earthq Eng 1991;10(8):386–401. http://dx.doi.org/10.1016/0267-7261(91)90053-3.

[31] Liu X, El Naggar MH, Wang KH, Wu JT. Three-dimensional axisymmetric analysis of pile vertical vibration. J Sound Vib 2021;494(1):115881. http://dx.doi.org/10.1016/j.jsv.2020.115881.

[32] Wu W, Wang K, Zhang Z, Leo C. Soil-pile interaction in the pile vertical vibration considering true three-dimensional wave effect of soil. Int J Numer Anal Methods Geomech 2013;37(17):2860–76. http://dx.doi.org/10.1002/nag.2164.

[33] Meng K, Cui CY, Liang ZM, Li HJ, Pei HF. A new approach for longitudinal vibration of a large-diameter floating pipe pile in visco-elastic soil considering the three-dimensional wave effects. Comput Geotech 2020;128:103840. http://dx.doi.org/10.1016/j.compgeo.2020.103840.

[34] Tsouvalas A, Metrikine AV. A semi-analytical model for the prediction of underwater noise from offshore pile driving. J Sound Vib 2013;332(13):3232–57. http://dx.doi.org/10.1016/j.jsv.2013.01.026.

[35] Jongmans D. Prediction of ground vibrations caused by pile driving: A new methodology. Eng Geol 1996;42(1):25–36. http://dx.doi.org/10.1016/0013-7952(95)00058-5.

[36] Masoumi H, Degrande G, Lombaert G. Prediction of free field vibrations due to pile driving using a dynamic soil–structure interaction formulation. Soil Dyn Earthq Eng 2007;27(2):126–43. http://dx.doi.org/10.1016/j.soildyn.2006.05.005.

[37] Hwang JH, Liang N, Chen CH. Ground response during pile driving. J Geotech Geoenviron Eng 2001;127(11):939–49. http://dx.doi.org/10.1061/(ASCE)1090-0241(2001)127:11(939).

[38] Dahl PH, Dall'Osto DR, Farrell DM. The underwater sound field from vibratory pile driving. J Acoust Soc Amer 2015;137(6):3544–54. http://dx.doi.org/10.1121/1.4921288.

[39] Talbot JP, Hunt HEM. A computationally efficient piled-foundation model for studying the effects of ground-borne vibration on buildings. Proc Inst Mech Eng Part C: J Mech Eng Sci 2003;217(9):975–89. http://dx.doi.org/10.1243/095440603322407227.

[40] Conto KF, Arcos R, Clot A, Ntotsios E, Liravi H, Colaço A, et al. A pile–soil interaction model for ground-borne vibration problems based on the singular boundary method. J Sound Vib 2024;568:118057. http://dx.doi.org/10.1016/j.jsv.2023.118057.

[41] van Dalen KN, Tsouvalas A, Metrikine AV, Hoving JS. Transition radiation excited by a surface load that moves over the interface of two elastic layers. Int J Solids Struct 2015;73:99–112. http://dx.doi.org/10.1016/j.ijsolstr.2015.07.001.

[42] Kachanov ML, Tsukrov I. Handbook of elasticity solutions. Springer Science & Business Media; 2003.

[43] Aki K, Richards PG. Quantitative seismology. University Science Books; 2002.

[44] Besserer H, Malischewsky PG. Mode series expansions at vertical boundaries in elastic waveguides. Wave Motion 2004;39(1):41–59. http://dx.doi.org/10.1016/S0165-2125(03)00069-6.

[45] Dellnitz M, Schütze O, Zheng QH. Locating all the zeros of an analytic function in one complex variable. J Comput Appl Mathe 2002;138(2):325–33. http://dx.doi.org/10.1016/S0377-0427(01)00371-5.

[46] Johnson T, Tucker W. Enclosing all zeros of an analytic function—A rigorous approach. J Comput Appl Mathe 2009;228(1):418–23. http://dx.doi.org/10.1016/j.cam.2008.10.014.

[47] Gillan CJ, Schuchinsky A, Spence I. Computing zeros of analytic functions in the complex plane without using derivatives. Comput Phys Com 2006;175(4):304–13. http://dx.doi.org/10.1016/j.cpc.2006.04.007.

[48] Madsen K. A root-finding algorithm based on Newton's method. BIT Numer Mathe 1973;13:71–5. http://dx.doi.org/10.1007/BF01933524.

[49] Martin D, Ahlfors L. Complex analysis. New York: McGraw-Hill; 1966.

[50] Stange S, Friederich W. Guided wave propagation across sharp lateral heterogeneities: the complete wavefield at a cylindrical inclusion. Geophys J Int 1992;111(3):470–82. http://dx.doi.org/10.1111/j.1365-246X.1992.tb02105.x.

[51] Zheng CJ, Kouretzis G, Ding X, Luan L. Vertical vibration of end-bearing single piles in poroelastic soil considering three-dimensional soil and pile wave effects. Comput Geotech 2022;146:104740. http://dx.doi.org/10.1016/j.compgeo.2022.104740.

[52] Mayes P. End stress calculations on elastic cylinders. Int J Solids Struct 1983;19(10):895–906. http://dx.doi.org/10.1016/0020-7683(83)90045-8.

[53] Bostock MG. On the orthogonality of surface wave eigenfunctions in cylindrical coordinates. Geophys J Int 1990;103(3):763–7. http://dx.doi.org/10.1111/j.1365-246X.1990.tb05688.x.

[54] Herrera I, Spence DA. Framework for biorthogonal Fourier series. Proc Nat Acad Sc 1981;78(12):7240–4. http://dx.doi.org/10.1073/pnas.78.12.724.

[55] Kuhlemeyer RL, Lysmer J. Finite element method accuracy for wave propagation problems. J Soil Mech Found Div 1973;99(5):421–7. http://dx.doi.org/10.1061/JSFEAQ.0001885.

[56] Bathe KJ, Wilson EL. Numerical methods in finite element analysis. Englewood Cliffs: Prentice Hall; 1976.

[57] Seed HB, Idriss IM, Lee KL, Makdisi FI. Dynamic analysis of the slide in the lower San Fernando Dam during the earthquake of February 9, 1971. J Geotech Eng Div 1975;101(9):889–911. http://dx.doi.org/10.1061/AJGEB6.0000195.

[58] Shan Z, Ling D. Analytical solution for the transient wave propagation of a buried cylindrical P-wave line source in a semi-infinite elastic medium with a fluid surface layer. J Sound Vib 2018;414:259–83. http://dx.doi.org/10.1016/j.jsv.2017.11.018.